the FEBS Journal

Structural role of the active-site metal in the conformation of *Trypanosoma brucei* phosphoglycerate mutase

Gustavo F. Mercaldi[1,*], Humberto M. Pereira[1], Artur T. Cordeiro[1,*], Paul A. M. Michels[2] and Otavio H. Thiemann[1]

1 Instituto de Física de São Carlos, Grupo de Cristalografia, Universidade de São Paulo, São Carlos, São Paulo, Brazil
2 Research Unit for Tropical Diseases, de Duve Institute and Laboratory of Biochemistry, Université Catholique de Louvain, Brussels, Belgium

Keywords
catallytic metal; gluconeogenic pathway; glycolytic pathway; phosphoglycerate mutase; *Trypanosoma brucei*

Correspondence
O. H. Thiemann, Instituto de Física de São Carlos, Grupo de Cristalografia, Universidade de São Paulo, CP 369, São Carlos, São Paulo 13560-970, Brazil
Fax: +55 16 3373 9881
Tel: +55 16 3373 8089
E-mail: thiemann@ifsc.usp.br

***Present address**
Laboratório Nacional de Biociências, Centro Nacional de Pesquisas em Energia e Materiais, Campinas, São Paulo 13083-100, Brazil

(Received 15 November 2011, revised 16 March 2012, accepted 26 March 2012)

doi:10.1111/j.1742-4658.2012.08586.x

Phosphoglycerate mutases (PGAMs) participate in both the glycolytic and the gluconeogenic pathways in reversible isomerization of 3-phosphoglycerate and 2-phosphoglycerate. PGAMs are members of two distinct protein families: enzymes that are dependent on or independent of the 2,3-bisphosphoglycerate cofactor. We determined the X-ray structure of the monomeric *Trypanosoma brucei* independent PGAM (*Tb*iPGAM) in its apoenzyme form, and confirmed this observation by small angle X-ray scattering data. Comparing the *Tb*iPGAM structure with the *Leishmania mexicana* independent PGAM structure, previously reported with a phosphoglycerate molecule bound to the active site, revealed the domain movement resulting from active site occupation. The structure reported here shows the interaction between Asp319 and the metal bound to the active site, and its contribution to the domain movement. Substitution of the metal-binding residue Asp319 by Ala resulted in complete loss of independent PGAM activity, and showed for the first time its involvement in the enzyme's function. As *Tb*iPGAM is an attractive molecular target for drug development, the apoenzyme conformation described here provides opportunities for its use in structure-based drug design approaches.

Database
Structural data for the *Trypanosoma brucei* 2,3-bisphosphoglycerate-independent phosphoglycerate mutase (iPGAM) has been deposited with the Research Collaboratory for Structural Bioinformatics (RCSB) Protein Data Bank under code 3NVL.

Structured digital abstract
- TbiPGAM and TbiPGAM bind by x-ray crystallography (View interaction)

Introduction

Phosphoglycerate mutases (PGAMs, EC 5.4.2.1) catalyze the reversible isomerization of 3-phosphoglycerate (3PGA) and 2-phosphoglycerate (2PGA) in the glycolytic and gluconeogenic pathways. Two evolutionarily distinct classes of PGAM have been described: cofactor (2,3-bisphosphoglycerate)-dependent dPGAMs and cofactor-independent iPGAMs [1]. iPGAMs are monomeric metalloenzymes with an absolute requirement for divalent metals that belong to the alkaline phosphatase superfamily and comprise a phosphatase

Abbreviations
2PGA, 2-phosphoglycerate; 3PGA, 3-phosphoglycerate; PGAM, phosphoglycerate mutase; dPGAM, 2,3-bisphosphoglycerate-dependent PGAM; iPGAM, 2,3-bisphosphoglycerate-independent PGAM; SAXS, small-angle X-ray diffraction.

 © 2012 The Authors Journal compilation © 2012 FEBS

and a transferase domain [2,3]. dPGAMs are usually dimeric or tetrameric, are not metalloenzymes belonging to the acid phosphatase superfamily. iPGAMs transfer the phospho group from 3PGA to 2PGA through a phosphoserine intermediate, while dPGAMs use a histidine residue as the transfer intermediate [4].

As mammalian cells only possess a dPGAM [5], whereas many pathogenic bacteria and protists possess an iPGAM, the latter has been proposed as a potential drug target for infectious diseases caused by these microorganisms [6–10]. At present, no potent and selective iPGAM inhibitors are known. Moreover, rational design of inhibitors based on molecular target structures has not yet proved feasible. iPGAM structures for the tropical parasite *Leishmania mexicana* [11] and various *Bacillus* species [3,6,12] co-crystallized with their natural substrates 3PGA/2PGA have been reported. When the active site is occupied by the substrate, the ligand is buried and is therefore inaccessible to the solvent. The only available ligand-free iPGAM crystal structure, from *Bacillus anthracis* (*Ba*iPGAM) (PDB accession code 2IFY), shows an open conformation that is different from holoenzyme structures. In this structure, there is a large separation between the two domains, and the catalytic residues are exposed to the solvent in a shallow polar site. Structural and molecular dynamic assessment between the two *Bacillus* iPGAMs was previously performed, leading to the conclusion that *Ba*iPGAM may have crystallized in a conformation that is somewhat different from the most favored one [6].

Trypanosoma brucei, which only possesses an iPGAM (*Tb*iPGAM) [13], belongs to the same Trypanosomatidae family as the *Leishmania* species. *T. brucei* is a parasitic protist that causes African trypanosomiasis, which is also called sleeping sickness in humans (caused by sub-species *T. b. gambiense* and *T. b. rhodesiense*) and 'nagana' in cattle (caused by the sub-species *T. b. brucei*), with devastating consequences for human health and livestock production in Africa. As for all mammalian pathogens of the Trypanosomatidae sub-species, lack of safe and effective drugs and the spread of strains resistant to the available drugs are driving the need for identification and characterization of biochemical targets as well as development of new drug candidates. Previous work has shown that *Tb*iPGAM is essential for the viability of both the bloodstream [8] and procyclic insect [14] forms of *T. brucei*, reinforcing the potential of the enzyme as a therapeutic target.

To further investigate *Tb*iPGAM, the recombinant enzyme was crystallized in the absence of 3PGA/2PGA, and its structure was solved at 2.3 Å resolution. *Tb*iPGAM was found in a novel open conformation in which the domains are slightly separated, distinct from that reported for the *Ba*iPGAM apoenzyme structure. In the new *Tb*iPGAM structure, the residue Asp319 from the transferase domain coordinated with the metal ion of the phosphatase domain. The Asp319 residue was replaced by Ala by site-directed mutagenesis, leading to complete loss of the enzyme activity. In this way, we show for the first time that the interaction of Asp319 with the *Tb*iPGAM metal ion is crucial for enzyme function. These data contribute to a deeper understanding of the flexibility and conformational changes of iPGAMs, shedding light on the functional and structural roles of the metal atom in these enzymes. Additionally, the *Tb*iPGAM structure offers a new opportunity for structure-based drug design approaches.

Results and Discussion

Protein isolation and characterization

The *Tb*iPGAM protein was expressed and purified to homogeneity by immobilized metal affinity and size-exclusion chromatography. The purified protein eluted in size-exclusion chromatography experiments as a 56 kDa monomer. Determination of its kinetic parameters for the substrate 3PGA resulted in a K_m value of 148 ± 17.7 μM and V_{max} and k_{cat} values of 19.6 ± 0.8 μM·min^{-1} and 3226 s^{-1}, respectively. These parameters are consistent with those previously reported and within the range for iPGAMs from other organisms [13], indicating that the recombinant *Tb*iPGAM represents the natural enzyme. In our assays, the specific activity of *Tb*iPGAM at 37 °C in the presence of cobalt was approximately 3 thousand International Units (IU) mg^{-1}, which represents a sevenfold increase in enzymatic activity compared previously published results [2], probably due to different experimental conditions.

Previous studies showed that *Tb*iPGAM was inactivated by metal-chelating agents such as EDTA, and reactivated by addition of divalent metals [13,15]. *In vivo*, Mg^{2+} and/or Zn^{2+} bound to the active site [2]. However, the presence of Co^{2+} led to hyperactivation of the enzyme *in vitro*, demonstrating that Co^{2+} has a high affinity for the enzyme compared to other metal ions. Additionally, in our crystallization experiments, we observed that divalent metal ions favor crystal growth, especially when cobalt was present. These observations indicate that metals play an essential role in iPGAM function as well as the enzyme conformation, as previously thought [2,6].

Crystal structure

The best crystallization conditions were achieved when 8 mg·mL^{-1} recombinant *Tb*iPGAM in 20 mM Tris/acetate/EDTA pH 7.4, 50 mM NaCl and 10 μM $CoCl_2$ was mixed 1 : 1 with precipitant solution comprising 0.05 M ammonium sulfate, 0.1 M Bis/Tris pH 6.1 and 25% w/v poly(ethylene glycol) 3350. Needle-like crystals of approximately 1.2 × 0.1 × 0.1 mm, belonging to monoclinic space group $P2_1$ with unit cell parameters of a = 62.67 Å, b = 85.66 Å, c = 109.11 Å, β = 102.2° were obtained. Statistical analysis of the merged reflections indicated that the collected dataset is best described as having a limiting resolution of 2.3 Å, with a total of 196 486 recorded reflections merged to 46 642 unique reflections. The overall completeness and R_{merge} correspond to 92.7% and 10%, respectively and 82.8% and 66% respectively, in the last shell.

Using the phosphatase and transferase domains of *Lm*iPGAM (Protein Data Bank ID 3IGY) independently as search models, we solved the *Tb*iPGAM structure by molecular replacement at 2.3 Å (Table 1). The asymmetric unit comprises two *Tb*iPGAM molecules related by a twofold non-crystallographic axis that contact each other at two distinct regions: one in a loop of the phosphatase domain, and the second in the transferase domain (Fig. 1A). PISA was used to investigate the molecular interaction surface of the macromolecular complex [16]. The calculate interface area was 760 Å^2, containing approximately 20 amino acids residues of each molecule that participate in four hydrogen bonds and one salt bridge. This analysis suggests that the monomer appears to be the biological relevant form as this interface is too small to favor the formation of a dimer in solution.

Two metal sites (M1 and M2) containing cobalt ions are present in the phosphatase domain of the *Tb*iPGAM structure (Fig. 1C). Likewise, the transferase domain contains a sulfate ion bound to a polar site exposed to the solvent (Fig. 1B), formed by residues His135, Val134, Arg165, Asp166, Arg201, Arg208, Arg281, Asp283 and Arg284. Additionally, a previously unknown cavity is formed between the *Tb*iPGAM transferase and phosphatase domains. The *Tb*iPGAM transferase and phosphatase domains, connected by two interdomain loops, have an α/β topology, with β-strands surrounded by α-helices (Fig. 1B). Individual alignment of the *Tb*iPGAM and *Lm*iPGAM domains resulted in a root mean square deviation (Cα-RMSD) of the phosphatase domain of 0.47 Å, and a Cα-RMSD of the transferase domain of 0.33 Å. Notwithstanding the domain similarity, overall structure alignment of *Tb*iPGAM and *Lm*iPGAM resulted in a Cα-RMSD of 8.32 Å. This indicates that the two molecules (*Tb*iPGAM and *Lm*iPGAM) have many differences, as shown in Fig. 3. Additionally, structural alignment of *Ba*iPGAM and *Tb*iPGAM demonstrates that these two apoenzyme structures also show significant differences (Fig. 3). In this case, the overall alignment resulted in a Cα-RMSD of 10.96 Å, with Cα-RMSDs of 0.94 and 1.14 Å for alignment of the phosphatase and transferase domains, respectively.

In addition to the conformational discrepancy between the *Ba*iPGAM and *Tb*iPGAM apoenzyme structures, an interaction was observed between the two domains of *Tb*iPGAM through coordination of the M1 metal site (phosphatase domain) by Asp319 (transferase domain), as show in Fig. 1B,C. This Asp319–metal interaction is apparently responsible for restricting the conformational flexibility of the enzyme and stabilizing the structure, consistent with the observation that the presence of divalent metal ions favored crystal growth in the crystallization experiments.

The conformational discrepancy between the ligand-free and ligand-bound forms of iPGAM corroborates the idea that iPGAMs have flexible hinges connecting

Table 1. Data collection and refinement statistics. Values in parentheses are given for the highest resolution shell (2.42–2.3 Å°). The R_{free} factor was calculated from a 5% subset of reflections removed randomly before the refinement.

Parameter	Value
Data collection	
Wavelength (Å)	1.4586
Resolution range (Å)	36.5–2.3
Total/unique reflections	196 486/46 642
Completeness (%)	92.7 (82.8)
R_{merge}	0.10 (0.66)
Redundancy	4.2
Mean I/σ (I)	9.2 (2.2)
Crystal	
Space group	$P2_1$
Cell dimension (Å)	
a	62.67
b	85.66
c	109.11
β (°)	102.2
Model refinement	
R factor/R_{free} factor†	0.16/0.21
RMSD bond length (Å)	0.004
RMSD bond angle (°)	0.8
Protein atoms	8518
Solvent atoms	237
Metal ions (Co^{2+})	4
Mean B-factor (Å^2)	36.5
PDB entry	3NVL

†R free-factor – calculated from a 5% subset of reflection removed randomly before the refinement.

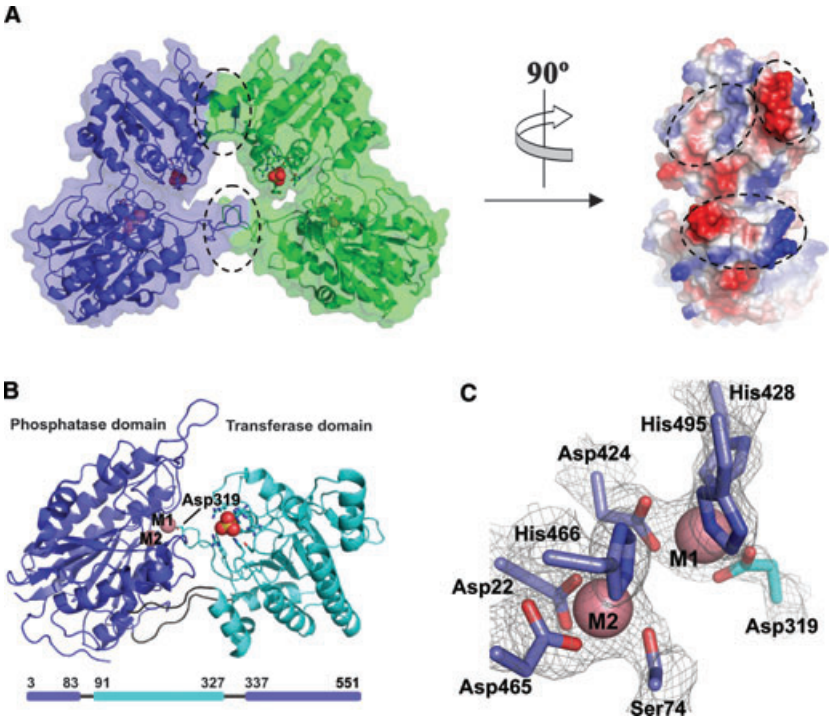

Fig. 1. Crystal structure of *Tbi*PGAM. (A) The asymmetric unit is formed by two *Tbi*PGAM molecules (colored blue and green). A 90° rotation showing the electrostatic surface of the monomer reveals that the contact area (highlighted) is predominantly polar. (B) The *Tbi*PGAM monomer is formed by the transferase and phosphatase domains connected by interdomain loops. A sulfate atom is bound to the transferase domain. Residue Asp319, located in a transferase domain loop, forms an electrostatic interaction with the cobalt ion located in the phosphatase domain. The diagram below is a representation of the amino acid sequence, colored according to the domain to which the residues belong. (C) Metal sites M1 and M2 are shown together with the residues that coordinate to the metal ions, colored according to their corresponding domains.

the phosphatase and transferase domains, and confirms that the mechanism of reaction for these enzymes requires a substrate-induced conformational change to accommodate the active site substrate [12,15].

Small-angle X-ray scattering (SAXS)

As note above, the *Tbi*PGAM crystallographic structure comprises two molecules in the asymmetric unit (Fig. 1A). However, PISA analysis and size-exclusion chromatography suggest that the enzyme behaves as a monomer. These contradictory results do not exclude possible transient dimer formation. To address this issue, we investigated the recombinant *Tbi*PGAM in solution by small-angle X-ray scattering (SAXS) experiments. The SAXS data revealed little interparticle interaction (Fig. 2A); additionally, the gyration radius (R_g) was similar (27.7 ± 0.2 Å) at all protein concentrations measured, leading to the conclusion that increasing the protein concentration does not result in *Tbi*PGAM oligomerization.

Comparison of the experimental SAXS and distance distribution function [P(r)] curves for ligand-free *Tbi*PGAM with the theoretical SAXS and P(r) curves generated for the dimer and monomer was performed (Fig. 2B), and a better fit to the theoretical curve was found for the monomer. Additionally, the distance distribution function P(r) shows that, under the experimental conditions, *Tbi*PGAM has a shape similar to the monomeric form, consistent with the conclusions from size-exclusion chromatography experiments and PISA contact area analysis that *Tbi*PGAM is a monomer.

Having established that each molecule of the asymmetric unit represents a monomer, we investigated whether conformational changes resulting from active-site occupation of iPGAMs could be detected in solution. Initially, we compared the P(r) and scattering curves from the monomeric structures of *Lmi*PGAM (closed conformation), *Bai*PGAM (open conformation) and *Tbi*PGAM (open conformation), which share highly conserved domain topologies (Fig. 2C). This

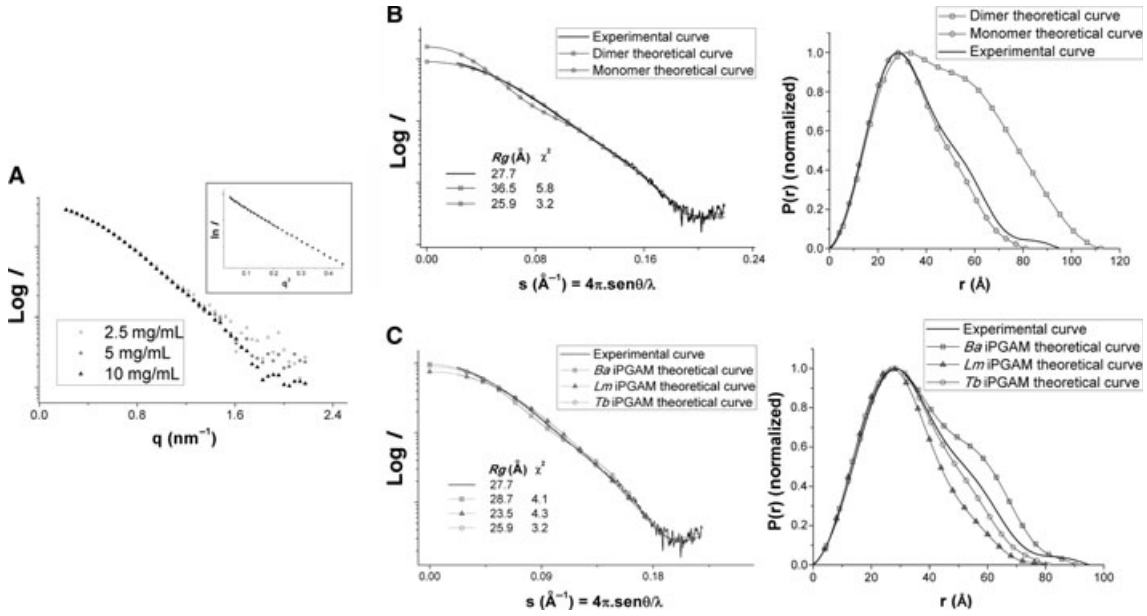

Fig. 2. Small-angle X-ray scattering analyses. (A) Experimental scattering curves for *Tb*iPGAM at various concentrations revealed that the oligomeric state is concentration-independent. The Guinier plot (inset) shows the absence of sample aggregation. (B) Superposition of experimentally and theoretically generated curves for the dimer and monomer of *Tb*iPGAM indicates that the recombinant enzyme is in the monomeric form in solution. (C) Superposition of theoretically and experimentally generated scattering curves for *Tb*iPGAM, *Ba*iPGAM and *Lm*iPGAM indicates that the *Tb*iPGAM open conformation was found in solution in the absence of substrate (or product). Examination of the P(r) curve shows that *Ba*iPGAM has a shape that is not observed for the experimental *Tb*iPGAM curve.

comparative analysis shows that the experimental curves fit slightly better the *Tb*iPGAM theoretical curve (see χ^2 in Fig. 2C). Although different conformations may be present in solution due to the domain flexibility of the apoenzyme iPGAM, apparently giving rise to a residual systematic error in curve fit, the P(r) curves show that the shape of *Tb*iPGAM differs from *Ba*iPGAM and also from *Lm*iPGAM. As expected, the *B. anthracis* enzyme has two well separated bodies (represented by the transferase and phosphatase domain), and *Lm*iPGAM has a globular shape. The *Tb*iPGAM experimental P(r) curve shows that the protein domains are separated, but they are not as distant as observed for *Ba*iPGAM (Fig. 2C). We conclude that the degree of flexibility of iPGAMs is constrained, corroborating the idea that Asp319–metal interaction restricts the conformation flexibility of the enzyme. Additionally, these results suggest that the open conformation observed in the crystallographic structure of *Tb*iPGAM is likely to be the biologically relevant conformation.

Ligand-induced conformational changes

Ligand-induced conformational changes of *Tb*iPGAM and *Lm*iPGAM were characterized using the DynDom program [17,18]. Superimposing the phosphatase domains (Fig. 1B), a 66.8° rotation and 0.8 Å translation was observed between the transferase domains of both iPGAMs (Fig. 3). Residues 87–89 and 328–335, located in the interdomain loops (Fig. 1B), are subject to large changes in the phi (φ) and psi (ψ) torsion angles to accommodate the domain movement.

The iPGAM active site comprises residues from both domains, and the catalytic residues are in close proximity to each other in the closed conformation. However, in the open conformation, the catalytic residues from the phosphatase and transferase domains are farther apart, exposing catalytic residues of the transferase domain to the solvent (Fig. 1B). Interestingly, the catalytic residues from the phosphatase domain involved in the M1 metal interaction are apparently unable to interact with ligands due to Asp319 coordination (Fig. 1B,C), but the M2 metal site remains available to interact with small molecules.

The Asp319–metal interaction prevents binding of molecules to catalytic residues of the phosphatase domain. This idea is reinforced by a previous study in which the ability of diethyl pyrocarbonate to irreversibly modify histidine residues was studied [19]. Complete diethyl pyrocarbonate protection of the catalytic histidine residues was reported in the presence

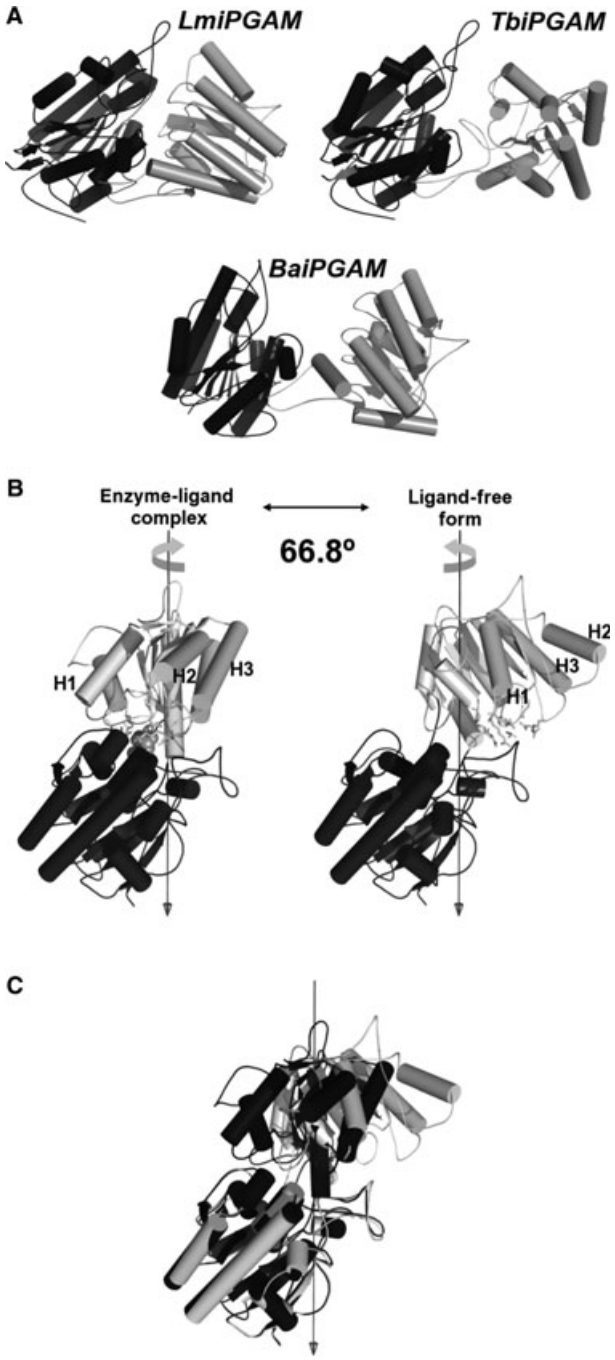

Fig. 3. Structural comparison of *Tb*iPGAM and *Ba*iPGAM (open conformations) and *Lm*iPGAM (closed conformation). (A) Structures of iPGAMs in various conformations. The phosphatase and transferase domains are colored dark and light gray, respectively. (B) The hinge axis is represented by the arrows. The phosphatase domain (dark gray) was kept fixed, and the transferase domain (light gray) was allowed to rotate along the hinge axis from the closed to the open structure, performing a 66.8° rotation as indicated by the curved arrow. (C) Superposition of the two molecules, highlighting the conformational discrepancy between the open (light gray) and closed (dark gray) conformations.

of 3PGA. This result is in agreement with the ligand-bound conformation of the previously solved iPGAM structures, in which all catalytic residues are buried and not exposed to solvent. Furthermore, in the absence of ligands, only two catalytic histidines (His136 and His467) are modified by diethyl pyrocarbonate [19], equivalent to the transferase domain His135 and the M2 site of the phosphatase domain His466 in the *Tb*iPGAM structure. This behavior can be explained by the *Tb*iPGAM conformation described here, whereby stabilization of the open structure resulting from interaction of Asp319 with the M1 metal protects the catalytic residues His495 and His428, but not His466 (Fig. 1C).

As the only catalytic residues available to interact with small molecules are those from the transferase domain, it is reasonable to speculate that the reaction of iPGAMs proceeds by substrate binding to transferase catalytic residues of the free enzyme. This substrate binding induces domain movement and trapping of the substrate in the active site of the closed conformation. Intramolecular transfer of the phospho group is accomplished through transitory formation of a phosphoserine intermediate, with the glyceric acid remaining bound to the enzyme until re-phosphorylated. Subsequently the product is released, leaving the protein in the open conformation.

The residues His135 and His466, as well as Asp319, are conserved in all available Trypanosomatidae iPGAM sequences (Fig. 4), and both histidines are essential for the enzyme's function [20]. These observations confirm that the apoenzyme *Tb*iPGAM structure is biologically relevant, and thus we decided to investigate the relevance of the M1 metal–Asp319 interaction.

In the holoenzyme iPGAMs, the residue corresponding to Asp319 in *Tb*iPGAM is exposed to the solvent and distant from the active site. However, in the apoenzyme *Tb*iPGAM, rotation of the transferase domain brings Asp319 close to the M1 site, allowing coordination of the M1 metal. Here, we demonstrate that substitution of Asp319 by Ala (*Tb*iPGAM-D319A) yields a soluble mutant with abolished enzyme activity (Fig. 5). Thus, we conclude that the M1 metal–Asp319 interaction plays a structural role in *Tb*iPGAM that is crucial for enzyme function. As previously discussed, the flexibility of apoenzyme iPGAMs is limited by the M1 metal–Asp319 interaction. It is hypothesized that an analogous result would be observed for other proteins of this enzyme class. However, Mg^{2+} and/or Zn^{2+} (not Co^{2+}) are the biologically relevant metal ions *in vivo*. Given this evidence regarding the structural role of metals for the iPGAMs, other biophysical

```
Tb  iPGAM  100-SGEIFTSEGYRYLHGAFSQ-PGRTLHLIGLLSDGGVHSRDNQVYQILKHAG-149
Tc  iPGAM  101-TGEIFTSDGYRYLHGAFSQ-PGRTLHLIGLLSDGGVHSRDNQLYEIINHAS-150
Lb  iPGAM  101-SGDIYTSEGYRYLHGSFCK-EGSTLHLIGLLSDGGVHSRDNQLYPIIEHAV-150
Ld  iPGAM  101-SGEIFTGEGYRYLLGAFSK-EDSTLHLIGLLSDGGVHSRDNQIYSIIERAA-150
Lm  iPGAM  101-SGEIYTGEGYRYLHGAFSK-EGSTLHLIGLLSDGGVHSRDNQIYSIIEHAV-150
Lmj iPGAM  101-SGEIYTGEGYRYLLGAFTK-EGSTLHLIGLLSDGGVHSRDNQIHSIIEHAA-150
An  iPGAM   98-KGELGKVDNIVASFKRAKEG-NGRLHLLGLVSDGGVHSNITHLVGLLKVAK-147
Pm  iPGAM  108-DGSMFKSKNFTHIVDELKDGSGRTLHLFGLLSDGNIHSNIAHVEKIVKEVA-152
                 *.: . ..         .  .  ***:**:***.:**.  ::  ::: .

Tb  iPGAM  300-FNRVRLPK-VRYAGMMRYDGDLGIPNNFLVPPPKLTRTSEEYLIGSGCNIF-349
Tc  iPGAM  301-FNRVRVPK-VRYAGMMRYDGDLGIPNNFLVPPPRLSRTSEEYLVGSGCNIF-350
Lb  iPGAM  301-FDRVRVPK-VRYAGMMRYDGDLGIPNNFLVPPPKLACVSEEYLCGTGLNIF-350
Ld  iPGAM  301-FDRVRVPK-VRYAGMMRYDGDLGIPNNFLVPPPKLTRVSEEYLCGSGLKIF-350
Lm  iPGAM  301-FDRVRVPK-VRYAGMMRYDGDLGIPNNFLVPPPKLTRVSEEYLCGSGLNIF-350
Lmj iPGAM  301-FDRVRVPK-VRYAGMMRYDGDLGIPNNFLVPPPKLTRVSEEYLCGTGLQIF-350
An  iPGAM  286-KPEFPYPKDIHITTMTRYKTDYTFPVAF--PPQHMGNVLAEWLGKKDVKQC-334
Pm  iPGAM  319-FDRRNAPK-VDYYGMLIYDNDQMIPKQSLAPNPDISHVLSEYMLAQGVKMY-368
                 .   ** :    *  *. *  :*     *   :  .  *::   . :

Tb  iPGAM  450-KEAVDSVNGVFLITADHGNSDDMVQRDKKGKPVRDAEGNLMPLTSHTLAPV-500
Tc  iPGAM  451-KEAVDAVNGVFLITADHGNSDDMAQRDKKGKPILGKDGKVLPLTSHTLAPV-501
Lb  iPGAM  451-KEAVDSVNGVFIVTADHGNSDDMAQRDKKGKPMKDEKGNVLPLTSHTLAPV-501
Ld  iPGAM  451-KDAVDNVNGVFIVTADHGNSDDMAQRDKKGKPIKDGKGNVLPLTSHTLSPV-501
Lm  iPGAM  451-KDAVDSVNGVYIVTADHGNSDDMAQRDKKGKPMKDGNGNVLPLTSHTLSPV-501
Lmj iPGAM  451-KDAVDSINGVFIVTADHGNSDDMAQRDKKGKPMKDEKGNVLPLTSHTLSPV-501
An  iPGAM  434-YEACKKHGYILFITADHGNAEEMLT----------EKG--TPKTSHTTNKV-472
Pm  iPGAM  470-VEAVTARNGIVVITADHGNCEEM----------KDKKGNI--KTSHTLNAI-508
                 :*    . : .:******.::*            .*     ****   :
```

Fig. 4. Sequence alignment of 2,3-bisphosphoglycerate-independent phosphoglycerate mutase (iPGAM) enzymes. The His135, Asp319 and His466 (numbering from *Tb*iPGAM) residues are underlined. Shown are *Tb* iPGAM from *T. brucei* (XP_823027.1); *Tc* iPGAM from *T. cruzi* (XP_820347.1); *Lb* iPGAM from *L. braziliensis* iPGAM (XP_001569313.1); *Ld* iPGAM from *L. donovani* iPGAM (ADG96010.1); *Lm* iPGAM from *L. Mexicana* iPGAM (CAD66620.1); *Lmj* iPGAM from *L. major* iPGAM (XP_001687258.1); *An* iPGAM from *Aspergillus niger* iPGAM (XP_001397611.1); *Pk* iPGAM from *Perkinsus marinus* iPGAM (XP_002774075). Numbers in parentheses are National Center for Biotechnology Information accession numbers. *, identical residues; ., conserved residues.

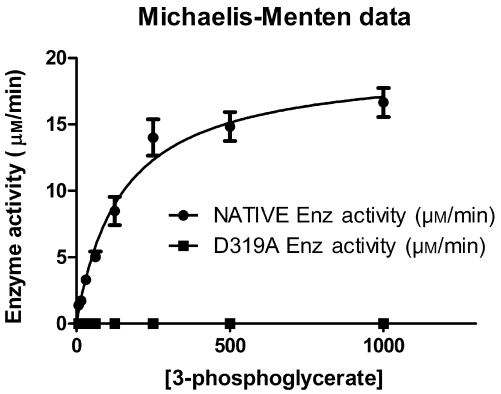

Fig. 5. Enzyme kinetics data for wild-type and mutant D319A forms of *Tb*iPGAM, confirming that the interaction between Asp319 and the M2 metal site is crucial for enzyme function. Even by increasing of the mutant enzyme concentration to 100 nM, there is no detectable catalytic activity.

and biochemical studies should be performed to confirm this hypothesis. Interestingly, the M1 site of trypanosomatid and plants has been described as the only site of iPGAMs found to contain a metal under physiological conditions [11].

Together, the data presented here reveal the ligand-induced conformational change during enzymatic catalysis of iPGAMs, and the new apoenzyme structure may contribute to efforts in to design iPGAM inhibitors with potential for clinical development as new trypanocidal drugs.

Experimental procedures

*Tb*iPGAM expression and purification

Escherichia coli BL21(DE3) strain cells harboring the recombinant pET28a-*Tb*iPGAM [13] plasmid were cultivated at 37 °C in Luria–Bertani broth containing 30 µg·mL^{-1} kanamycin and 1 M sorbitol until an attenuance of 0.8 (at 600 nm) was reached. The culture was subjected to a heat-shock process [21] followed by overnight induction with isopropyl thio-β-D-galactoside. Cells

were harvested by centrifugation (800 ***g*** for 15 min at 4 °C) and suspended in 30 mL of lysis buffer containing 50 mM NaH_2PO_4/NaOH pH 7.0, 0.6 M NaCl, 1 mM KH_2PO_4, 5 mM $MgCl_2$, 10 mM imidazole, 0.5 mM Tris(2-carboxyethyl)phosphine/HCl, 0.4 mM phenylmethanesulfonyl fluoride, 10 μM leupeptin, 1 μM pepstatin, and 10% glycerol. Cell disruption was achieved using a French Press cell disrupter (one cycle, 20 000 psi). Benzonase and protamine sulfate were added, and the cell lysate was clarified by centrifugation at 2000 ***g*** for 30 min at 4 °C. *Tb*iPGAM was purified to homogeneity using 1 mL metal affinity resin (Talon; Clontech, Mountain View, CA, USA) pre-equilibrated with the lysis buffer, and the recombinant *Tb*iPGAM was eluted using lysis buffer containing 50 mM imidazole. The sample containing *Tb*iPGAM was dialyzed in buffer A containing 50 mM triethanolamine/HCl (TEA) pH 7.5, 150 mM NaCl and 10 μM $CoCl_2$. Purified *Tb*iPGAM at 5 $mg{\cdot}mL^{-1}$ was analyzed by size-exclusion chromatography using a Superdex 200 GL 10/30 column (GE Healthcare, Piscataway, NJ, USA) in buffer A at a flow rate of 1 $mL{\cdot}min^{-1}$.

Enzyme kinetics

The *Tb*iPGAM activity was measured by coupling the isomerization of 3PGA to 2PGA to lactate dehydrogenase using enolase and pyruvate kinase. NADH consumption was monitored at 37 °C in a 96-well plate reader, measuring the decrease in absorbance at 340 nm, with a final assay volume of 0.2 mL per well. The reaction mixture contained 0.1 M triethanolamine (pH 7.4), 0.1 M NaCl, 1 mM $MgSO_4$, 1 mM ADP, 0.5 mM NADH, 10 μM $CoCl_2$ and 20 IU in $mg{\cdot}mL^{-1}$ of the auxiliary enzymes lactate dehydrogenase, enolase and pyruvate kinase. All reagents were purchased from Sigma-Aldrich (St Louis, MO).

Determination of the K_m for 3PGA for *Tb*iPGAM was performed using an enzyme concentration of 0.1 nM, and varying the concentration of 3PGA from 1 mM to 7.8 μM (serial dilution). Data were obtained from three independent experiments. The Michaelis–Menten constant was estimated by fitting a curve by non-linear regression.

Crystallization and data collection

*Tb*iPGAM crystallization conditions were screened using a Honeybee 931 robot (Genomic Solutions Inc., Ann Arbor, MI, USA) and eight Hampton Research (Aliso Viejo, CA, USA) and Qiagen Inc. (Valencia, CA, USA) screening kits at 18 °C. The best *Tb*iPGAM crystallization conditions, after refinement of the initial conditions, were 18 °C using droplets of 3 μL protein solution at 8 $mg{\cdot}mL^{-1}$ in 20 mM Tris/acetate/EDTA pH 7.4, 50 mM NaCl, 10 μM $CoCl_2$ and 3 μL reservoir solution containing 0.05 M ammonium sulfate, 0.1 M Bis/Tris pH 6.1, and 25% w/v poly(ethylene glycol) 3350 by the hanging-drop method. A total of 300 images with 0.7° rotation were collected using the W01B-MX2 beamline of the Brazilian National Laboratory of Synchrotron Light (Campinas, Brazil) using a MAR Mosaic 225 CCD detector (Marresearch GmbH, Norderstedt, Germany) at 135 mm distance (Table 1).

Structure determination and refinement

Diffraction data were indexed and integrated using MOSFLM [22] and scaled using SCALA [23] from the CCP4 suite [24]. The structure was initially solved by molecular replacement with Phaser [25], using the transferase and phosphatase domains of *Lm*iPGAM (Protein Data Bank ID 3IGY) independently as the search models. Refinement was performed using a combination of PHENIX [26] and REFMAC [27]. Model building was performed using Coot [28]. The final structure was refined to 2.3 Å resolution. All statistics are shown in Table 1.

Small-angle X-ray scattering

SAXS data were collected using the D02A-SAXS2 beam line of Brazilian National Laboratory of Synchrotron Light with a sample-to-detector distance of 1.543 m, 1.488 Å wavelength and 300 s exposures at *Tb*iPGAM concentrations of 2.5, 5.0 and 10.0 $mg{\cdot}mL^{-1}$ in 50 mM TEA pH 7.5, 150 mM NaCl, 10 μM $CoCl_2$ and 5% glycerol. Scattering from the buffer was measured and subtracted from the protein sample data, and the images were integrated using FIT2D version 12.077 (http://www.esrf.fr/computing/scientific/FIT2D/) to obtain the scattering curves.

PRIMUS [29] was used to assess interparticle interference, evaluate aggregation and determine the gyration radius (*Rg*) by the Guinier method [30]. GNOM 4.5 [31] was used to obtain the distance distribution function P(r) and *Rg* in real space by indirect Fourier transform. Finally, Crysol [32] was applied to evaluate the theoretical solution-scattering curve of *Tb*iPGAM, *Lm*iPGAM and *Ba*iPGAM monomers, using the available crystallographic structures.

Site-directed mutagenesis

Substitution of Asp319 for an Ala residue, generating clone *Tb*iPGAM-D319A, was performed using a QuikChange site-directed mutagenesis kit (Stratagene, La Jolla, CA, USA), according to the manufacturer's instructions, with primer pairs D319A_f (5′-GATGCGCTACGATGGTGCG TTGGGTATTCCTAACAAC-3′) and D319A_r (5′-GTTG TTAGGAATACCCAACGCACCATCGTAGCGCATC-3′). Underlining indicates the mutation site.

Acknowledgements

We would like to thank Malcolm D. Walkinshaw (Institute of Structural and Molecular Biology, The

University of Edinburgh, Edinburgh, UK) and Linda A. Fothergill-Gilmore (Department of Biochemistry, University of Edinburgh, Edinburgh, UK) for sharing *Lmi*PGAM structures before they were publicly available, and the members of the Protein Crystallography and Structural Biology Group at the Instituto de Física de São Carlos, Universidade de São Paulo, Brazil, for helpful discussions during the course of this work, and to express our gratitude to Dr Susana A. Sculaccio, José A. L. da Costa, José G. Catarino and Norma B. Saes for technical help during this study. The work was supported in part by research grant 575933/2008-9 from the Conselho Nacional de Desenvolvimento Científico e Tecnológico (CNPq) and research grant 06/55686-4 from the Fundação de Amparo à Pesquisa do Estado de São Paulo (FAPESP) to O.H.T. G.F.M. received a master degree scholarship from CNPq, and H.M.P. and A.T.C. received FAPESP post-doctoral fellowships at the Instituto de Física de São Carlos, Universidade de São Paulo.

References

1 Foster JM, Davis PJ, Raverdy S, Sibley MH, Raleigh EA, Kumar S & Carlow CK (2010) Evolution of bacterial phosphoglycerate mutases: non-homologous isofunctional enzymes undergoing gene losses, gains and lateral transfers. *PLoS One* **5**, e13576.

2 Fuad FA, Fothergill-Gilmore LA, Nowicki MW, Eades LJ, Morgan HP, McNae IW, Michels PA & Walkinshaw MD (2011) Phosphoglycerate mutase from *Trypanosoma brucei* is hyperactivated by cobalt *in vitro*, but not *in vivo*. *Metallomics* **3**, 1310–1317.

3 Rigden DJ, Lamani E, Mello LV, Littlejohn JE & Jedrzejas MJ (2003) Insights into the catalytic mechanism of cofactor-independent phosphoglycerate mutase from X-ray crystallography, simulated dynamics and molecular modeling. *J Mol Biol* **328**, 909–920.

4 Rigden DJ, Mello LV, Setlow P & Jedrzejas MJ (2002) Structure and mechanism of action of a cofactor-dependent phosphoglycerate mutase homolog from *Bacillus stearothermophilus* with broad specificity phosphatase activity. *J Mol Biol* **315**, 1129–1143.

5 Carreras J, Mezquita J, Bosch J, Bartrons R & Pons G (1982) Phylogeny and ontogeny of the phosphoglycerate mutases. IV. Distribution of glycerate-2,3-P2 dependent and independent phosphoglycerate mutases in algae, fungi, plants and animals. *Comp Biochem Physiol* **71**, 591–597.

6 Nukui M, Mello LV, Littlejohn JE, Setlow B, Setlow P, Kim K, Leighton T & Jedrzejas MJ (2007) Structure and molecular mechanism of *Bacillus anthracis* cofactor-independent phosphoglycerate mutase: a crucial enzyme for spores and growing cells of *Bacillus* species. *Biophys J* **92**, 977–988.

7 Zhang Y, Foster JM, Kumar S, Fougere M & Carlow CK (2004) Cofactor-independent phosphoglycerate mutase has an essential role in *Caenorhabditis elegans* and is conserved in parasitic nematodes. *J Biol Chem* **279**, 37185–37190.

8 Albert MA, Haanstra JR, Hannaert V, Van Roy J, Opperdoes FR, Bakker BM & Michels PA (2005) Experimental and *in silico* analyses of glycolytic flux control in bloodstream form *Trypanosoma brucei*. *J Biol Chem* **280**, 28306–28315.

9 Foster JM, Raverdy S, Ganatra MB, Colussi PA, Taron CH & Carlow CK (2009) The Wolbachia endosymbiont of *Brugia malayi* has an active phosphoglycerate mutase: a candidate target for anti-filarial therapies. *Parasitol Res* **104**, 1047–1052.

10 Poonperm B, Guerra DG, McNae IW, Fothergill-Gilmore LA & Walkinshaw MD (2003) Expression, purification, crystallization and preliminary crystallographic analysis of *Leishmania mexicana* phosphoglycerate mutase. *Acta Crystallogr D Biol Crystallogr* **59**, 1313–1316.

11 Nowicki MW, Kuaprasert B, McNae IW, Morgan HP, Harding MM, Michels PA, Fothergill-Gilmore LA & Walkinshaw MD (2009) Crystal structures of *Leishmania mexicana* phosphoglycerate mutase suggest a one-metal mechanism and a new enzyme subclass. *J Mol Biol* **394**, 535–543.

12 Jedrzejas MJ, Chander M, Setlow P & Krishnasamy G (2000) Structure and mechanism of action of a novel phosphoglycerate mutase from *Bacillus stearothermophilus*. *EMBO J* **19**, 1419–1431.

13 Chevalier N, Rigden DJ, Van Roy J, Opperdoes FR & Michels PA (2000) *Trypanosoma brucei* contains a 2,3-bisphosphoglycerate independent phosphoglycerate mutase. *Eur J Biochem* **267**, 1464–1472.

14 Djikeng A, Raverdy S, Foster J, Bartholomeu D, Zhang Y, El-Sayed NM & Carlow C (2007) Cofactor-independent phosphoglycerate mutase is an essential gene in procyclic form *Trypanosoma brucei*. *Parasitol Res* **100**, 887–892.

15 Collet JF, Stroobant V & Van Schaftingen E (2001) The 2,3-bisphosphoglycerate-independent phosphoglycerate mutase from *Trypanosoma brucei*: metal-ion dependency and phosphoenzyme formation. *FEMS Microbiol Lett* **204**, 39–44.

16 Krissinel E & Henrick K (2007) Inference of macromolecular assemblies from crystalline state. *J Mol Biol* **372**, 774–797.

17 Hayward S, Kitao A & Berendsen HJ (1997) Model-free methods of analyzing domain motions in proteins from simulation: a comparison of normal mode analysis

and molecular dynamics simulation of lysozyme. *Proteins* **27**, 425–437.
18 Hayward S & Berendsen HJ (1998) Systematic analysis of domain motions in proteins from conformational change: new results on citrate synthase and T4 lysozyme. *Proteins* **30**, 144–154.
19 Guerra DG, Vertommen D, Fothergill-Gilmore LA, Opperdoes FR & Michels PA (2004) Characterization of the cofactor-independent phosphoglycerate mutase from Leishmania mexicana mexicana: histidines that coordinate the two metal ions in the active site show different susceptibilities to irreversible chemical modification. *Eur J Biochem* **271**, 1798–1810.
20 Huang Y & Dennis DT (1995) Histidine residues 139, 363 and 500 are essential for catalytic activity of cofactor-independent phosphoglyceromutase from developing endosperm of the castor plant. *Eur J Biochem* **229**, 395–402.
21 Oganesyan N, Ankoudinova I, Kim SH & Kim R (2007) Effect of osmotic stress and heat shock in recombinant protein overexpression and crystallization. *Protein Expr Purif* **52**, 280–285.
22 Leslie AGW & Powell HR (2007) Processing diffraction data with MOSFLM. In *Evolving Methods for Macromolecular Crystallography* (Read RJ & Sussman JL eds), pp. 41–51. IOS Press/Springer, Amsterdam, The Netherlands.
23 Evans P (2006) Scaling and assessment of data quality. *Acta Crystallogr D Biol Crystallogr* **62**, 72–82.
24 Bailey S (1994) The Ccp4 suite – programs for protein crystallography. *Acta Crystallogr D Biol Crystallogr* **50**, 760–763.
25 McCoy AJ (2007) Solving structures of protein complexes by molecular replacement with Phaser. *Acta Crystallogr D Biol Crystallogr* **63**, 32–41.
26 Adams PD, Grosse-Kunstleve RW, Hung LW, Ioerger TR, McCoy AJ, Moriarty NW, Read RJ, Sacchettini JC, Sauter NK & Terwilliger TC (2002) PHENIX: building new software for automated crystallographic structure determination. *Acta Crystallogr D Biol Crystallogr* **58**, 1948–1954.
27 Murshudov GN, Vagin AA & Dodson EJ (1997) Refinement of macromolecular structures by the maximum-likelihood method. *Acta Crystallogr D Biol Crystallogr* **53**, 240–255.
28 Emsley P & Cowtan K (2004) Coot: model-building tools for molecular graphics. *Acta Crystallogr D Biol Crystallogr* **60**, 2126–2132.
29 Konarev PV, Volkov VV, Sokolova AV, Koch MHJ & Svergun DI (2003) PRIMUS: a Windows PC-based system for small-angle scattering data analysis. *J Appl Crystallogr* **36**, 1277–1282.
30 Svergun DI & Koch MHJ (2003) Small-angle scattering studies of biological macromolecules in solution. *Rep Prog Phys* **66**, 1735–1782.
31 Semenyuk AV & Svergun DI (1991) Gnom – a program package for small-angle scattering data-processing. *J Appl Crystallogr* **24**, 537–540.
32 Svergun D, Barberato C & Koch MHJ (1995) CRYSOL – a program to evaluate X-ray solution scattering of biological macromolecules from atomic coordinates. *J Appl Crystallogr* **28**, 768–773.